# On the use of machine learning algorithms for the calibration of astigmatism PTV

## Christian Cierpka[1]*, Jörg König[1], Minqian Chen[2], David Boho[2], Patrick Mäder[2]

[1] Technische Universitt Ilmenau, Institute of Thermodynamics and Fluid Mechanics, Ilmenau, Germany

[2] Technische Universitt Ilmenau, Group for Software Engineering for Safety-Critical Systems, Ilmenau, Germany

* christian.cierpka@tu-ilmenau.de

## Abstract

Microfluidic devices become more an more popular in many chemical, process engineering and biological applications. The fluidic channels in these devices have typical dimensions of several ten to hundred micrometer. In order to measure the three-dimensional velocity field, where volume illumination and out-of-plane gradients are sources of major bias errors, astigmatism particle tracking has become a valuable tool to circumvent these biases (Cierpka and Kähler, 2012) and is widely used for different applications (e.g. Liu et al. (2014); Holtzer et al. (2007); Rossi et al. (2011)). The principle is based on a cylindrical lens placed within the observation light path and the determination of the elliptical distortion of the particle images (Cierpka et al., 2011b; Rossi and Kähler, 2014). Since the system relies only on the addition of the cylindrical lens, it allows for a cheap and easy extension of traditional fluorescence microscopes into systems capable to measure the volumetric three component velocity field. For a calibration, usually particle images from particles placed on several known distances in front of the objective lens are evaluated and a parametric fit function for the particle images width and height with depth position is determined (Cierpka et al., 2011a). This procedure strongly relies on the evaluation of single particle images that may be taken in different illumination conditions and are subjected to image aberrations and noise. Therefore, the estimated width and height show a certain scatter for particles located at the same depth position depending on the particle size, the signal-to-noise ratio, position within the field of view, variations in laser light intensity, etc.. Depending on the experimental conditions, this may add up to a random error for the position measurement in depth direction of up to several percent of the total measurement range. To obtain a more robust and reliable calibration function and to cope with overlapping particle images, recent advances in the field of machine vision offer new possibilities. The present study, therefore, aims to compare classical data evaluation and calibration by image processing with machine learning approaches for APTV.

## 1 Introduction

### 1.1 Astigmatism particle tracking velocimetry

Microfluidic devices show a high potential in several fields including chemical processing, medical science, biology and energy conversion among others. Very often the fluid flow is strongly three-dimensional. Modern velocity measurement techniques such as particle image velocimetry (PIV) or particle tracking velocimetry (PTV) are very often applied. The flow is seeded with tracer particles and illuminated by laser light. On the one hand the laser illumination usually results in an illumination of the whole fluid volume due to the small scales on the other hand the flow can only be observed from one direction via microscopes. In order to measure the three-dimensional velocity field astigmatism particle tracking (APTV) uses astigmatic optical aberrations caused by the introduction of a cylindrical lens in the light path (Cierpka et al., 2011b; Rossi and Kähler, 2014). For a calibration, usually particle images from particles placed on several known distances in front of the objective lens are evaluated and a parametric fit function for the particle images width and height with depth position is determined (Cierpka et al., 2011a). For that procedure the width

and the height of individual particle images have to be determined reliably. Since the particle images may have been taken in different illumination conditions and are subjected to additional image aberrations and noise, the estimated width and height show a certain scatter for particles located at the same depth position. This uncertainty depends on the particle size, the signal-to-noise ratio, position within the field of view, variations in laser light intensity among others. Depending on the experimental conditions, this may add up to a random error for the position measurement in depth direction of up to several percent of the total measurement range. Furthermore, a high seeding concentration is beneficial for a dense spacing of the final velocity vectors. A high seeding concentration usually results into a considerable amount of overlapping particle images that are difficult to detect by standard image processing.

## 1.2 Deep neural networks for image annotation and flow measurements

To obtain a more robust and reliable calibration function and to cope with overlapping particle images, recent advances in the field of machine vision pose a new approach. Machine learning algorithms are a powerful tool in classifying images. In previous work, a technique was developed that automatically identifies 2,770 German plant species and builds upon latest deep learning approaches. Achieving accuracies well beyond 80% on a single plant image in this extremely fine-grained classification problem impressively demonstrate the potential of machine learning (Seeland et al., 2019; Wäldchen and Mäder, 2018; Wäldchen et al., 2018). (Dunker et al., 2018), utilized deep learning techniques to classify the species and the age of phytoplankton captured in microscopic images with a cytometer. To be successfully applied to the calibration problem in particle tracking, such algorithms have to be trained with a set of training images with known depth position. Once the network is trained, the algorithm is capable of determining classes within a set of actual images although large deviations of the individual images due to the above mentioned issues are present. The big advantage of neural networks is that no specific knowledge about the process to analyze is necessary from a first point of view and the algorithms are robust even for very noisy images. However, a large amount of already annotated training data is required to train the network. Furthermore, for the training data the classes or structures to look for have to be obtained by classical tools. The increasing computer performance, already available pretrained networks and their large applicability to different problems have let to an increased use for fluid dynamic purposes.

Grant and Pan (1995) were among the first studies using neural networks for the determination of the fluid velocity via PTV and PIV. In the first approach, already multi-layer beural networks (three and four layer) were used to determine the particle image displacement in successive frames. The images in this early work were not analyzed by the network but using classical image processing methods. The particle image center positions were fed within a binary image into the network. The amount of correctly matched particle images in these studies were always larger than for classical methods in low seeding concentration images (50 to 500 particle images in double exposure per image). Later the same authors used networks to classify between overlapped and non-overlapped particle images to exclude outliers (Grant and Pan, 1997). Using cellular neural networks for PTV higher matching probability at low computational time was found by Ohmi and Sapkota (2006). Recently deep convolutional networks were used to determine the velocity vectors in densely seeded flows (Cai et al., 2019; Lee et al., 2017). Since for training different flows (wall bounded, bluff body, uniform) were used, the algorithm was capable to be applied to a variety of flow situations. Although the results are quite promising, the computational cost were much larger than using classical correlation methods. However, machine learning algorithms are a powerful tool in classifying the particle images itself and were already used for macroscopic APTV using large particles ($O(1\,\mathrm{mm})$) and extract Gaussian features of the corresponding particle images (Franchini et al., 2019). Deep networks were recently also applied to analyze flow features as for example turbulent superstructures in a flow with heat transfer based on their footprint in the temperature field (Fonda et al., 2019). The ever increasing performance of these networks will not only help to analyze flow features, but also to improve measurement techniques in the near future. The aim of the study is therefore, to quantitatively determine if a deep convolutional neural network yields better results for an image analysis and calibration of APTV measurements. The final particle pairing will be done with advanced classical algorithms described in Cierpka et al. (2013).

## 1.3 Preliminary test

To test if a deep neural network can be useful for the calibration of microscopic APTV images, a first preliminary study using experimentally calibration images was performed. For this reason a particle solution was placed on a microscope slide and imaged via a microscopic setup using an additional cylindrical lens ($f = 200\,\mathrm{mm}$). Since particle images in this first test will be attributed to a certain class (in this case depth

position), about 12,000 individual particle images at depth positions between 0 $\mu$m and 96 $\mu$m with a step size of 3 $\mu$m, resulting in 33 classes, were produced. The particle positions for this first test were determined using classical image preprocessing (Cierpka et al., 2011a). The images were than cropped around the particle image positions to yield sub-images with 180 $\times$ 180 pixel. By the known distance of particles images, sub-images with more than one particle image as well as particle images cut by the boarder of the whole image were excluded. The whole set of 11,807 sub-images was subdivided into 80% of the individual particle images for training, 10% for a validation and another 10% for actual testing. From these about 1,200 particle images for testing 97.54% were correctly matched with the right class, i.e. the correct depth information. For the remaining part the correct class was among the first three most probable classes which gives space to an optimization and was due to the image noise since real experimental images were used. As the application of the deep neural network was successfully shown, synthetic particle images, where the ground truth is known and the signal-to-noise ratio can be varied, will be presented in section 2. The final aim of the current study, using synthetic images, is to determine systematically the robustness, accuracy and limitations of the approach in comparison to classical image analysis in section 3.

## 2 Synthetic test case

### 2.1 Image generator

In order to have particle images with known ground truth a synthetic particle image generator was applied. The algorithm is based on the mathematical background derived by Rossi and Kähler (2014) and generates particle images from the known optical setup including (magnification, focal length of the cylindrical lens, distance of the camera, wavelength of the light, refractive index of the medium, etc.). In the current case particle images were produced for a typical setup using a magnification of 20 and a focal length of 200 mm for the cylindrical lens. The final distance between the two focal planes of the APTV setup was 40 $\mu$m. The particle image width and height using the in-house particle image detection software resulted in a size distribution between 20 and 100 pixels. The vertical distance was varied from 0 to 90 $\mu$m in steps of 1 $\mu$m. In total 150 calibration images for each vertical position were created. For each of the calibration images a random number of more than 8 particle images were randomly distributed over a 2560 $\times$ 2175 pixel space to avoid overlapping particle images to a good extend. This results in a total number of about 8 $\times$ 150 $\times$ 91 $\sim$ 110,000 individual particle images.
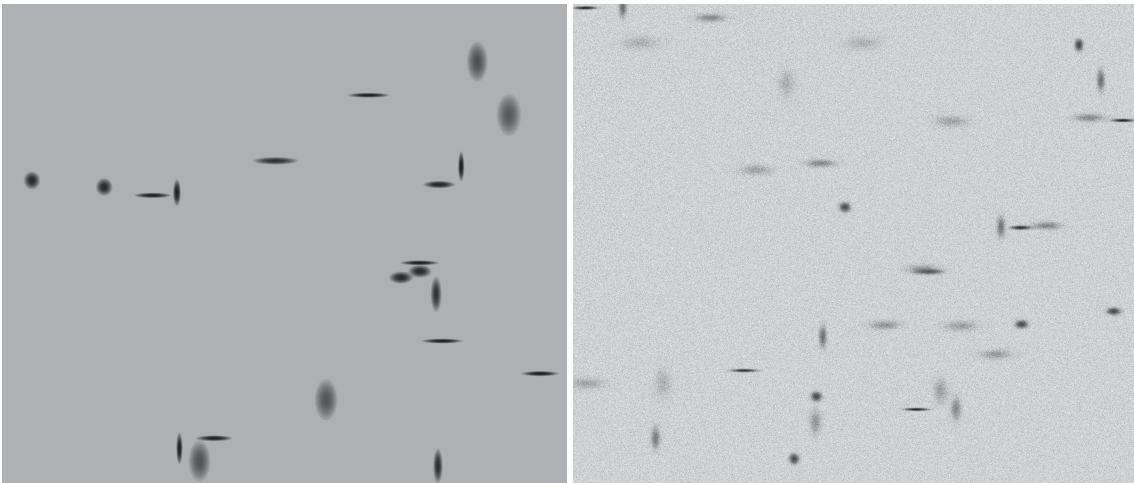


Figure 1: Synthetic particle images without noise (left) and with random noise with an SNR = 1 (right).

For the simulation of a typical measurements scenario same settings were used and 1,000 images with more than 20 individual particle images in each of them were generated which corresponds to a particle concentration of about $2 \times 10^{-3}$ vol. %. The particle positions were varied from -14 $\mu$m to 104 $\mu$m, since in reality very often smaller volumes were successively measured in a larger channel to increase the spatial resolution in the depth direction. For these images the signal-to-noise-ratio (SNR) was varied from no noise to SNR = 1 to 1,000. The SNR is defined as the squared mean intensity of the pixels divided by the

noise power. In order to generate noisy particle images, the mean intensity of the illuminated pixels was determined. Based on the mean intensity the variance of the noise was set according to the definition of the SNR applying the SNR level prescribed for each data set. Finally, Gaussian white noise with zero mean intensity and the determined variance was added to the images. In Fig. 1 the final images without noise (left) and with random noise with an SNR = 1 (right) can be seen. For better visibility the images were inverted and the contrast was enhanced.

## 2.2 Classical image processing

For the image processing the same settings were used for the synthetic images with and without noise. For preprocessing a Gaussian smoothing using a $9 \times 9$ pixel kernel and a $\sigma$ of 5 were used, followed by a median subtraction using a $3 \times 3$ pixel kernel. For the detection of regions where particle images might exist a global threshold of 10 counts was applied. The width and the height of the particle images were allowed to vary between 12 and 250 pixels to cover a broad range. For the in-plane position and the width and height sub-pixel accuracy was reached using a correlation with a Gaussian (Cierpka and Kähler, 2012).

To exclude strong outliers from the boarder of the image due to half cut particle images only particle images with a center position distance of at least 100 pixels to either boarder are considered valid. Since such a criterion can also be used in real measurements on the basis of the detected particle images this is a valid procedure. No other outlier filters were used to remove for example results from partly overlapping images as can be seen in Fig.1. Therefore, in total 94,363 individual particle images were taken for the calibration as described in greater detail in Cierpka et al. (2011a).

## 2.3 Shallow neural networks for data fitting

A second approach is to train shallow neural networks to fit features that were extracted by classical image processing as mentioned above. A similar approach was already used to determine temperatures by fitting the Hue value of thermochromic liquid crystals (Moller et al., 2019). The main benefit is, that the robust image processing that was already proven to yield reproducible results can be used and no model function for the optical behavior must be considered. That means, even if the theoretical change of the width and the height of the particle images over depth position is not known and valuable results can be achieved, even when the actual change of width and height differs strongly from the theoretical one due to large optical aberrations for example.

In order to test such a system a shallow network with three hidden layers and a small number of neurons (10 for the first layer, 30 for the second layer and 5 for the third layer) was used. For the training 80% of the data from the same data set as obtained from the classical image processing was used taking *AX* and *AY* as input. The Matlab toolbox for fitting with neural networks was used for training using standard parameters. The network was trained from scratch for ten times and the training state with the lowest deviation between estimated and real Z-position was taken for the calibration.

## 2.4 Deep neural network

The final aim of using a deep neural network is to apply the method to the whole processing chain. Therefore the particle image annotation shall be done by a faster region convolutional network (R-CNN). The idea of a faster R-CNN is that, if there are two CNNs, the first one is used to generate the region proposals to find each candidate image for the particles. The second is the classification of candidate regions and bounding-box regression. If there is only one CNN, two specific tasks can be launched simultaneously, which saves time. The first few layers need to calculate the convolution. If they are allowed to share the parameters, their own specific objectives and tasks are achieved only in the last few layers. Then, an image can use these shared convolution layers for only one forward propagation and, at the same time, can also find the region proposals, classification, and bounding-box regression (Ren et al., 2015).

The input of the Region Proposal Network (RPN) is an image of any size, and the output is a set of object proposals. RPNs use a small network to perform a sliding scan on a convolutional feature map, which is the last shared convolutional layer. Through this sliding window, the convolutional feature map is mapped to a low-dimensional feature (256 in Fig.2), which is an intermediate layer. Finally, the low-dimensional feature is fed into the two sibling fully connected layers. Namely, a box-regression layer and a box-classification layer. The centre of each sliding window corresponds to k anchor boxes, which are associated with a scale and aspect ratio. There are three scales (128, 256, 512) and three ratios (1:1, 1:2, 2:1). So, each sliding window has nine anchors. The box-regression layer predicts the parameter of the proposal region

corresponding to each anchor, which is $(X, Y, AX, AY)$. The box-classification layer determines whether the proposal region is in the foreground (object) or the background (non-object). The structure of the Region Proposal Networks is shown in Fig. 2.

As can be seen the Faster R-CNN uses shared convolutional layers so that region proposals are computationally cost-effective. Furthermore, unlike the traditional Region-of-interest generation method, such as a selective search achieved by using a CPU, RPNs can be implemented on a GPU.
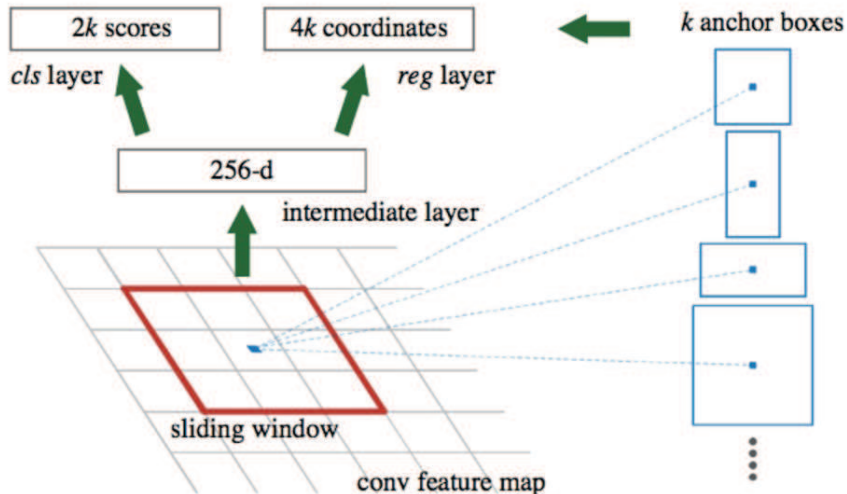


Figure 2: Region Proposal Network. The centre of each sliding window is corresponding to k anchor boxes with three scales and three ratios.

The implementation of this strategy was done as follows: ResNet-101/citeHe2015, a standard deep neural network architecture was used to extract features from the input image tensor. Batch normalization was used for all feature extractors after the convolutional layers. The optimizer for Faster R-CNN is asynchronous SGD with momentum of 0.9. The initial learning rate was $3 \times 10^{-4}$ and the learning rate is reduced by $10\times$ after 900K iterations and then $10\times$ after 1.2M iterations. For weight initialization, a truncated normal initializer was used with a standard deviation of $\sigma = 0.01$. In order to prevent the typical overfitting problem for smaller samples, L2 Regularization was added. Because an object should be equally recognizable as its mirror image, it is necessary to flip an image. At this point, horizontal flipping of an image as data augmentation was used for the faster R-CNN. The particle image depth regression was implemented using Keras. Inception V3 (Szegedy et al., 2015), a standard deep neural network architecture, was used to extract features from the input image tensor. The initial learning rate was set to 0.01. The optimizer for depth regression is Adam with exponential decay. The initial learning was fed into the exponential decay, and at each epoch the learning rate was reduced by 2.4. In total the number of training epochs was 800 and the batch size was set to 32.

## 3 Results

To test the applicability of the process the calibration data was used to determine a calibration and calculated the mean absolute error (mae) from the difference between the estimated and the known depth position mae $= \langle |Z_{\mathrm{est}} - Z_{\mathrm{real}}| \rangle$, where $\langle \ldots \rangle$ indicates the average. For the calibration data with the classical method the mean average error is mae $= 0.046 \, \mu m$. In Fig. 3 the estimated depth position $Z_{\mathrm{est}}$ vs. the actual known depth position $Z_{\mathrm{real}}$ for the synthetic calibration data is shown for the case of the classical image processing on the upper left side. The red line corresponds to a perfect match between both values. As can be seen for the classical image processing most of the points lie in the vicinity of the true value. Some strong outlier can be seen especially between both focal planes at $25 \leq Z \leq 65 \, \mu m$. However these outliers most often have a large Euclidian distance to the calibration curve and could be removed by the application of a filter (see
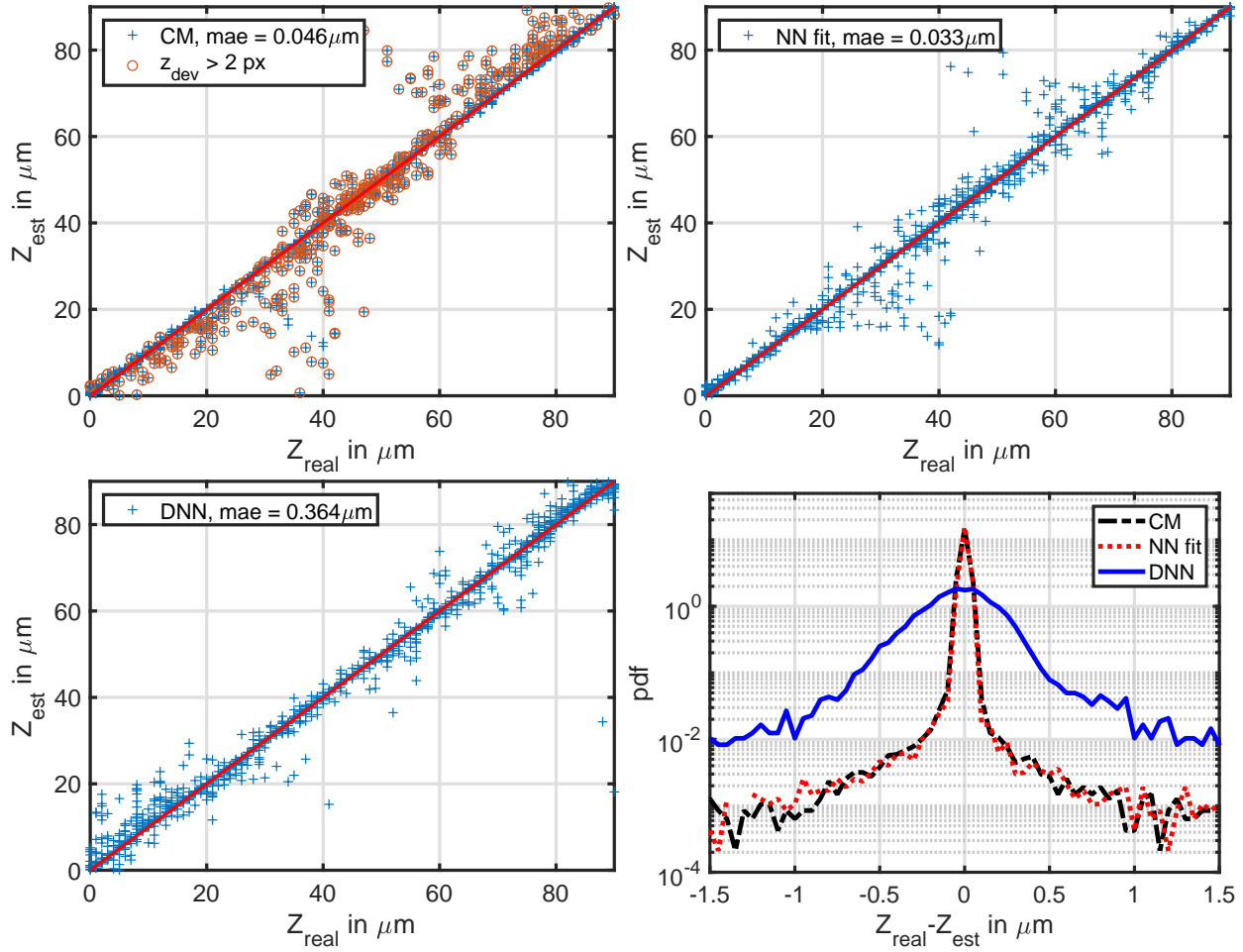
Figure 3: Estimated depth position $Z_{est}$ vs. actual depth position $Z_{real}$ for classical image processing (upper left), the fit with a shallow neural network (upper right) and the use of the deep neural network (lower left). The red circles in the upper left part show particle images that have a distance of more than 2 pixels from the calibration curve. Probability density function of the deviation between estimated depth position $Z_{est}$ and actual depth position $Z_{real}$ for classical image processing (black dash-dot line), the fit with the shallow neural network (red dotted line) and the use of the deep neural network (blue line).

for example figure 6 in (Cierpka et al., 2011a)). The red circles for example indicate particle images that would be excluded if a maximal distance of 2 pixels would be allowed. For the calibration with the classical methods using the outlier filter mae reduces to mae $= 0.024\,\mu$m, excluding in total about 12% of the data. Since this filter is not available for the deep neural network, it was not applied in the following analysis. However, despite some strong outliers the calibration matches the known depth position quite well.

The fit with the shallow neural network is shown on the right side of the upper row. The mean average deviation is even lower (mae $= 0.033\,\mu$m). Some outliers can also be seen here, especially close to the focal planes, where the change in width and height with deft position is low.

For the deep neural network the data for training (i.e. the calibration data) cannot be used to estimate the error since the algorithm would take the exact position known from the training. Therefore 10% of the calibration data was not used for training and can now be taken to estimate the mean absolute error to be mae $= 0.364\,\mu$m. This value is a factor of 8 larger in comparison to the other methods. On the lower left part of Fig. 3 it can be seen that the distance of the points to the line for an ideal match is in general a bit larger without showing strong outliers than the other methods. A similar behavior can be seen at the probability density function of the deviation from the true value which is shown in the same figure on the lower right part.

The pdf for the classical image processing (black dash-dot line) and the fit with a shallow neural network

(red dotted line) show similar distributions with a high probability of a very low deviation. The probability for a deviation of $\pm 0.5 \mu$m is already three orders of magnitude lower than the maximum value in the center. The pdf for the deep neural network (blue line) shows a bit broader distribution which means small and large deviations have a considerable high probability. However, the maximum is in the center, i.e. at low deviations, which means that the technique in general is applicable and further improvements can help to optimize the results.
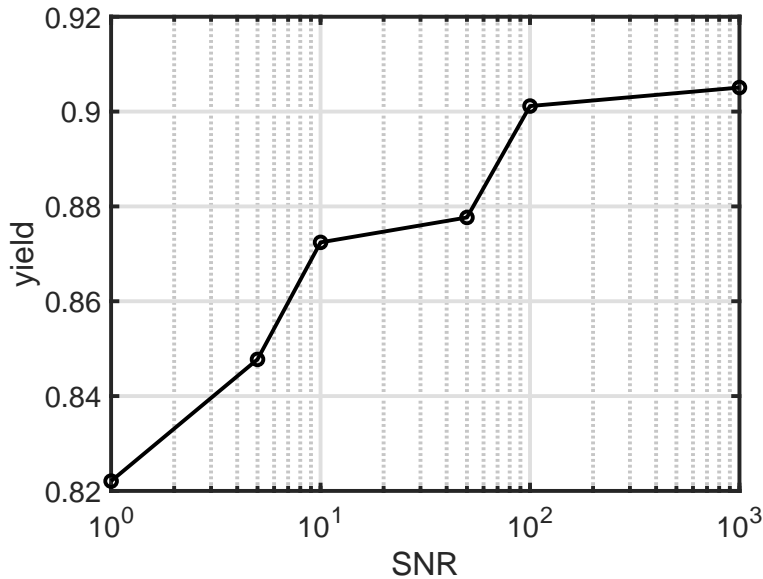


Figure 4: Yield for classical image processing.

The processing for the randomly distributed particle images with and without noise was done using the same parameters for the classical image preprocessing and the deep neural network, respectively. Within one image more individual particle images from different depth position were present and the number of overlapping particles increases (Cierpka et al., 2013). This and the increasing noise level reduces the number of valid detections. Since the determination of the width and height is now also subjected to a higher uncertainty the calibration results as well as the in-plane positions show higher uncertainties. Since a direct assignment of the detected and simulated images is not possible a particle tracking approach was used to determine the distance between a simulated and a detected particle image. In the case of a perfect match the distance would be zero for all three directions. The probabilistic particle tracking algorithm was used (Cierpka et al., 2013) allowing a maximum displacement of $\pm 10$ pixels for the in-plane direction. Since the in-plane position can be extracted with much lower uncertainty the PTV approach was forced to determine the in-plane distance with a much larger priority by premultiplying the Z-values with $10^{-5}$. For the later analysis the proper range was restored.

In Fig. 4 the yield calculated as ratio between the actual valid determined particle images pairs divided by the number of simulated particle images is shown. As can be seen for the lowest SNR using the above mentioned data processing for the classical method yield in about 82% of valid detected particle pairs. This value increases with increasing SNR up to 90.5% for the images without noise. It has to be mentioned that this number depends strongly on the settings. Since within this study only the depth position was of interest, the yield for both methods would be the same. However, in a later approach also the in-plane position shall be determined by a neural network which may increase the yield significantly, especially for the cases with higher noise level.

For the data of the processsing with the deep neural network the out-of-plane position could be directly compared to the real value since the actual positions were taken from the synthetic image generator. Therefore not particle tracking had to be applied. This means no errors due to wrong particle pairing are present in the data. However, if particles overlap they most often show a strong deviation from the real depth position. These particle images would be filtered by the pairing approach, which would result in a lower amount of strong outliers for the classical data processing in comparison to the deep neural network.

In Fig. 5 the mean absolute error for all directions for the classical image processing and fit with a shallow neural network can be seen over SNR. For the images without noise the lines indicate mae $\leq 0.03$
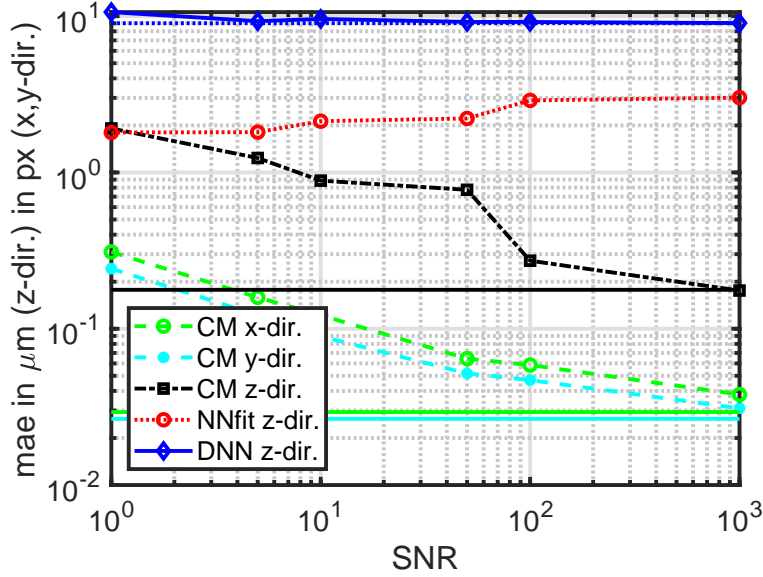
Figure 5: Mean absolute error (mae) determined from all distances between evaluated particle positions to known particle positions for different coordinate directions for classical image processing (blue, red, black curves) and the use of the deep neural network (cyan curve).

pixel for the in-plane direction using the classical image processing. The deviation increases by one order of magnitude to mae $\approx 0.3$ pixel for an SNR of 1. For the out-of-plane direction the mae $\leq 0.18\,\mu m$ for the case without noise (which is a factor of 4 larger than for the calibration data) and mae $\approx 1.9\,\mu m$ for an SNR of 1 are determined using the classical image processing. For the uncertainty usually the standard deviation is taken as a first estimate. For SNR = 1 $\sigma_Z = 2.5\,\mu m$ which corresponds to $\pm 2.8$ % of the measurements range. For the case without noise the value reduces to $\pm 0.4$ %. For the calibration with the shallow neural network the mean absolute error is in the order of mae $\approx 1.8\ldots 3.0\,\mu m$ with no clear trend. By inspecting the distribution of the error it can be seen that the largest deviation appears at the boundary in depth direction, i.e. at 0 and 90 $\mu m$. However, it seems that the error is quite stable over SNR. Using the deep neural network on the testing data results in mae $= 9.01\,\mu m$ for the case without noise (which is a factor of 18 larger than for the calibration data). This is much larger than for the preliminary test case. However, even for large noise levels this value stays about constant. For an SNR of 1 the mean absolute deviation is mae $= 10.62\,\mu m$, thus the mae is not affected by the SNR in the same way as the classical image processing, where the mae increases about a factor of 10 from the case without noise to the case with SNR = 1. However, the standard deviation is in the order of $\sigma_Z \approx 16\,\mu m$ for all test cases. This would result in an uncertainty of 18% and has to be improved in future studies.

## 4   Conclusion

It was shown that machine learning algorithms and deep neural networks can be applied to determine the particle positions using APTV. However, using classical image processing a very low mean absolute error of only 0.046 $\mu m$ was determined, whereas the training of a deep neural network based on the images gives for the same data a mean absolute error of 0.08 $\mu m$. Using classical image processing an a fit by a shallow neural network results in an even lower mean absolute deviation of only 0.033 $\mu m$ which was the lowest value reached in the current investigation. However, the good results for the classical image processing can be explained as the underlying model function was also used for the image generation. If this function would not be known due to strong aberrations or non-spherical particles shallow neural networks could be used to fit features extracted by classical image processing. So far this approach results in mean absolute errors that were always better than the classical image processing with a classical calibration. It has to be stated again that another benefit for this approach is that no a-priory knowledge of the calibration function has to fed into the model.

The results for the deep neural network are not yet in the same order of magnitude. However, it was

shown that the deep neural network is very robust to noise. Since image noise is always problematic, especially in microfluidics, this might be a valuable option after further improvement on the training parameters. Using the deep neural network on the other hand as well for the image annotation has the benefit, that even less knowledge in image preprocessing and image analysis is necessary and the technique is very robust to noise. Therefore it may be used more frequently by researchers from different fields. The results may also be applied to any other three-dimensional method relying on particle image variation with depth direction (Cierpka and Kähler, 2012) and will therefore be of general use. It would also be possible to use non-spherical randomly shaped and oriented particles like bacteria, cells, or proteins as typically examples for biological applications (Barnkob et al., 2015). Not only the velocity determination but also a clustering of types of particles may be possible within one data evaluation step. This opens a broad applicability.

## Acknowledgements

## References

Barnkob R, Kähler CJ, and Rossi M (2015) General defocusing particle tracking. *Lab on a Chip* 15:3556–3560

Cai S, Zhou S, Xu C, and Gao Q (2019) Dense motion estimation of particle images via a convolutional neural network. *Experiments in Fluids* 60:73

Cierpka C and Kähler C (2012) Cross-correlation or tracking comparison and discussion. in *International Symposium on Applications of Laser Techniques to Fluid Mechanics, 09.-12.07.2, Lisbon, Portugal*

Cierpka C and Kähler CJ (2012) Particle imaging techniques for volumetric three-component (3D3C) velocity measurements in microfluidics. *Journal of Flow Visualization* 15:1–31

Cierpka C, Lütke B, and Kähler CJ (2013) Higher order multi-frame Particle Tracking Velocimetry. *Experiments in Fluids* 54:1533

Cierpka C, Rossi M, Segura R, and Kähler CJ (2011a) On the calibration of astigmatism particle tracking velocimetry for microflows. *Measurements Science and Technology* 22:015401

Cierpka C, Rossi M, Segura R, Mastrangelo F, and Kähler CJ (2011b) A comparative analysis of the uncertainty of astigmatism-$\mu$PTV, stereo-$\mu$PIV, and $\mu$PIV. *Experiments in Fluids*

Dunker S, Boho D, Wldchen J, and Mder P (2018) Combining high-throughput imaging flow cytometry and deep learning for efficient species and life-cycle stage identification of phytoplankton. *BMC Ecology* 18:51

Fonda E, Pandey A, Schumacher J, and Sreenivasan KR (2019) Deep learning in turbulent convection networks. *Proceedings of the National Academy of Sciences* 116:8667–8672

Franchini S, Charogiannis A, Markides CN, Blunt MJ, and Krevor S (2019) Calibration of astigmatic particle tracking velocimetry based on generalized gaussian feature extraction. *Advances in Water Resources* 124:1 – 8

Grant I and Pan X (1995) An investigation of the performance of multi layer, neural networks applied to the analysis of piv images. *Experiments in Fluids* 19:159–166

Grant I and Pan X (1997) The use of neural techniques in PIV and PTV. *Measurement Science and Technology* 8:1399–1405

Holtzer L, Meckel T, and Schmidt T (2007) Nanometric three-dimensional tracking of individual quantum dots in cells. *Applied Physics Letters* 90:053902

Lee Y, Yang H, and Yin Z (2017) PIV-DCNN: cascaded deep convolutional neural networks for particle image velocimetry. *Experiments in Fluids* 58:171

Liu Z, Speetjens MFM, Frijns AJH, and van Steenhoven AA (2014) Application of astigmatism$\mu$-ptv to analyze the vortex structure of ac electroosmotic flows. *Microfluidics and Nanofluidics* 16:553–569

Moller S, Resagk C, and Cierpka C (2019) Anwendung neuronaler Netze zur Temperaturfeldmessung in Rayleigh-Bnard Konvektion mittels thermochromer Flssigkristalle. in *Fachtagung "Lasermethoden in der Strömungsmesstechnik", Erlangen, September, 3-5*

Ohmi K and Sapkota A (2006) Cellcell neural network based ptv. in *13th Int. Symp. on Applications of Laser Techniques to Fluid Mechanics*. Lisbon, Portugal, 26-29 June

Ren S, He K, Girshick RB, and Sun J (2015) Faster R-CNN: towards real-time object detection with region proposal networks. *Computing Research Repository* abs/1506.01497

Rossi M, Cierpka C, Segura R, and Kähler CJ (2011) Volumetric reconstruction of the 3D boundary of stream tubes with general topology using tracer particles. *Measurements Science and Technology* 22:105405

Rossi M and Kähler CJ (2014) Optimization of astigmatic particle tracking velocimeters. *Experiments in Fluids* 55:1809

Seeland M, Rzanny M, Boho D, Wäldchen J, and Mäder P (2019) Image-based classification of plant genus and family for trained and untrained plant species. *BMC Bioinformatics* 20:4

Szegedy C, Vanhoucke V, Ioffe S, Shlens J, and Wojna Z (2015) Rethinking the Inception Architecture for Computer Vision. *Computing Research Repository* abs/1512.00567

Wäldchen J and Mäder P (2018) Machine learning for image based species identification. *Methods in Ecology and Evolution* 9:2216–2225

Wäldchen J, Rzanny M, Seeland M, and Mäder P (2018) Automated plant species identificationtrends and future directions. *PLOS Computational Biology* 14:1–19